# CHITAH: STRONG-GRAVITATIONAL-LENS HUNTER IN IMAGING SURVEYS

JAMES H. H. CHAN[1,2], SHERRY H. SUYU[2], TZIHONG CHIUEH[1,3,4], ANUPREETA MORE[5], PHILIP J. MARSHALL[6], JEAN COUPON[7],
MASAMUNE OGURI[8,9,10], AND PAUL PRICE[11]

[1] Department of Physics, National Taiwan University, 10617 Taipei, Taiwan; d00222002@ntu.edu.tw
[2] Institute of Astronomy and Astrophysics, Academia Sinica, P.O. Box 23-141, Taipei 10617, Taiwan
[3] Institute of Astrophysics, National Taiwan University, 10617 Taipei, Taiwan
[4] Center for Theoretical Sciences, National Taiwan University, 10617 Taipei, Taiwan
[5] Kavli IPMU (WPI), UTIAS, The University of Tokyo, Kashiwa, Chiba 277-8583, Japan
[6] Kavli Institute for Particle Astrophysics and Cosmology, Stanford University, 452 Lomita Mall, Stanford, CA 94035, USA
[7] Astronomical Observatory of the University of Geneva, ch. d'Ecogia 16, 1290 Versoix, Switzerland
[8] Kavli Institute for the Physics and Mathematics of the Universe (Kavli IPMU, WPI), University of Tokyo, 5-1-5 Kashiwanoha, Kashiwa-shi, Chiba 277-8583, Japan
[9] Research Center for the Early Universe, University of Tokyo, 7-3-1 Hongo, Bunkyo-ku, Tokyo 113-0033, Japan
[10] Department of Physics, University of Tokyo, 7-3-1 Hongo, Bunkyo-ku, Tokyo 113-0033, Japan
[11] Department of Astrophysical Sciences, Princeton University, Princeton, NJ 08544, USA
Received 2014 November 17; accepted 2015 May 26; published 2015 July 7

## ABSTRACT

Strong gravitationally lensed quasars provide powerful means to study galaxy evolution and cosmology. Current and upcoming imaging surveys will contain thousands of new lensed quasars, augmenting the existing sample by at least two orders of magnitude. To find such lens systems, we built a robot, CHITAH, that hunts for lensed quasars by modeling the configuration of the multiple quasar images. Specifically, given an image of an object that might be a lensed quasar, CHITAH first disentangles the light from the supposed lens galaxy and the light from the multiple quasar images based on color information. A simple rule is designed to categorize the given object as a potential four-image (quad) or two-image (double) lensed quasar system. The configuration of the identified quasar images is subsequently modeled to classify whether the object is a lensed quasar system. We test the performance of CHITAH using simulated lens systems based on the Canada–France–Hawaii Telescope Legacy Survey. For bright quads with large image separations (with Einstein radius $r_{ein} > 1\farcs1$) simulated using Gaussian point-spread functions, a high true-positive rate (TPR) of $\sim$90% and a low false-positive rate of $\sim$3% show that this is a promising approach to search for new lens systems. We obtain high TPR for lens systems with $r_{ein} \gtrsim 0\farcs5$, so the performance of CHITAH is set by the seeing. We further feed a known gravitational lens system, COSMOS 5921 +0638, to CHITAH, and demonstrate that CHITAH is able to classify this real gravitational lens system successfully. Our newly built CHITAH is omnivorous and can hunt in any ground-based imaging surveys.

*Key words:* gravitational lensing: strong – methods: data analysis – quasars: individual (anguita)

## 1. INTRODUCTION

Strong gravitational lensing occurs when light emitted from a source is deflected by a foreground lens object, resulting in multiple images. Although lens systems are quite rare, we can use them to measure the mass distribution of foreground objects, from galaxies to galaxy clusters. Moreover, the signal from background source objects is magnified so we can make use of this information to probe the high-redshift universe.

The first strong gravitational lens system, Q0957+561, was discovered by Walsh et al. (1979). This two-image lensed object provided the first opportunity to study cosmology through strong lensing tools. Since then, there have been many searches through imaging or spectroscopic surveys for lenses. However, most of them are aimed at detecting lensed galaxies rather than lensed quasars, including the Sloan Lens Advanced Camera for Surveys (ACS) Survey (e.g., Bolton et al. 2006), the CFHTLS[12] Strong Lensing Legacy Survey (e.g., Cabanac et al. 2007; Gavazzi et al. 2012; More et al. 2012), the BOSS Emission-line Lens Survey (BELLS; e.g., Brownstein et al. 2012), the *Hubble Space Telescope* (*HST*) Archive Galaxy-scale Gravitational Lens Search (HAGGLeS; Marshall et al. 2009), *Herschel* ATLAS (H-ATLAS; e.g., Negrello

et al. 2010), and the South Pole Telescope (e.g., Vieira et al. 2013). Through these surveys, there are now a couple of hundred strong lenses with different source populations. We expect that bigger samples will be discovered in ongoing imaging surveys (Oguri & Marshall 2010), such as the Hyper Suprime-Cam (HSC) Survey (Miyazaki et al. 2012) and the Dark Energy Survey (DES) (Sánchez & DES Collaboration 2010).

Lensed quasars, although rarer than lensed galaxies, provide powerful means to study both galaxy evolution and cosmology. For galaxy evolution, we can study galaxy mass structures and substructures through the use of the positions, shapes, and fluxes of lensed images (e.g., Dalal & Kochanek 2002; Suyu et al. 2012; Vegetti et al. 2012). For cosmology, measuring time delays between multiple images allows us to determine the time-delay distance, which is sensitive to the Hubble constant, $H_0$ (e.g., Refsdal 1964; Suyu et al. 2010, 2013; Courbin et al. 2011; Tewes et al. 2013). This quantity is one of the crucial cosmological parameters that sets the age, size, and critical density of the universe. By combining the time delays with the stellar velocity dispersion of the lens, we can also measure the angular diameter distance to the lens for cosmological studies (e.g., Paraficz & Hjorth 2009; Jee et al. 2014).

Since lensed quasars are very useful, there have been several undertakings to look for them with various suverys. The Cosmic Lens All-sky Survey (Myers et al. 2003) discovered

---

[12] Canada–France–Hawaii Telescope Legacy Survey. See http://www.cfht.hawaii.edu/Science/CFHLS/ and links therein for a comprehensive description.

the largest statistical sample of radio-loud gravitational lenses by obtaining high-resolution images of flat-spectrum radio sources and identifying the ones that showed multiple images. In the optical, the SDSS Quasar Lens Search (e.g., Oguri et al. 2006, 2008, 2012; Inada et al. 2008, 2010, 2012) has obtained the largest lensed quasar sample to date based on both morphological and color selection of spectroscopically confirmed quasars. Jackson et al. (2012) further combined the quasar samples from the SDSS and the UKIRT Infrared Deep Sky Survey to find small-separation or high-flux-ratio lenses. Another systematic approach has been proposed by Kochanek et al. (2006) where all extended variable sources are identified as potential lenses. Recently, Agnello et al. (2015) proposed a novel way to select lens candidates through machine-learning algorithms.

We focus on an independent and effective way to detect lens systems automatically via modeling the quasar image configurations, as first demonstrated by Marshall et al. (2009) who detected lenses in the *HST* archival images via lens modeling as part of HAGGLeS. The philosophy of HAGGLeS is that for a lens candidate to be considered as such, its imaging data must be able to be explained by a lens model. Therefore, they use a Singular Isothermal Sphere (SIS) as lens mass profile plus external shear to fit the observed images of candidate lens objects. However, the HAGGLeS robot aims at detecting lensed galaxies rather than lensed quasars. Inspired by HAGGLeS, we build a robot, CHITAH, to search for lensed quasars in imaging surveys via modeling.

CHITAH is an acronym for Chung-li He In-hsiang Tan Ao Hao, which is a direct transliteration from 重力和影像探奥號 that means a robot for explorations of gravitational imaging. This robot is able to measure the positions of the lens galaxy and the multiple quasar images. We also employ a Singular Isothermal Ellipsoid (SIE) and a SIS as lens mass profiles to identify lenses with four-image and two-image configurations of quasar images (also known as "quads" and "doubles"), respectively.

We design CHITAH with multi-filter, high-resolution, and signal-to-noise imaging data in mind, i.e., the HSC Survey and the Large Synoptic Survey Telescope (LSST). The separation of the lens galaxy and quasar components for the modeling will depend on data quality, and other approaches may be better suited to poorer quality imaging data (e.g., LensTractor; P. J. Marshall et al. 2015, in preparation).

This paper is organized as follows. In Section 2, we detail the procedure of how CHITAH classifies lens candidates. We describe the simulated lenses based on CFHTLS data for educating CHITAH in Section 3, and present the results of the training in Section 4. We demonstrate that CHITAH can successfully identify a real gravitational lens in Section 5. We conclude in Section 6. Magnitudes quoted in this paper are in AB magnitudes.

## 2. CHITAH: LENS FINDING ROBOT

The criterion for selecting a lensed system is based on the configuration of the quasar images. Therefore, we have to separate lens galaxy and quasar images, and then identify the quasar image positions. To separate lens and quasar images, we can make use of their color information. For simplicity, we use two imaging bands for constructing the color. We illustrate the method with $g$ and $z$ bands (which are frequently available from large-scale imaging surveys), but the method can be applied to any other two bands, provided they are sufficiently separated in wavelength to distinguish the different colors of the lens galaxies and quasars.

There are four different scenarios of lensed objects depending on their colors and brightnesses, and we list the four cases in Table 1. The most typical situation of a lensed object is Case 1: quasar images are bluer and the lens galaxy is brighter in the $z$-band. To build a versatile robot, we try to cover all four situations of lensed objects. In the following subsections, we describe our procedure that works for all cases, and illustrate it with two typical examples of Case 1, one quad and one double, shown in Figures 1 and 2, respectively.

### 2.1. Separation of Lens and Quasars

Since the color is different between the lens galaxy and quasar images, below we describe a procedure to use cutouts of the lens system in $g$-band and $z$-band to produce two images: one containing only the lens galaxy, and another containing the lensed quasars only.

(a) Match up the point-spread function (PSF) in $g$ and $z$ bands, since the PSF is generally different between bands. Specifically, we seek to determine the kernel function, $K$, such that

$$\mathrm{PSF}_g = K * \mathrm{PSF}_z, \tag{1}$$

where $\mathrm{PSF}_g$ and $\mathrm{PSF}_z$ are the PSFs in $g$-band and $z$-band, respectively. Here we assume the typical situation where $\mathrm{PSF}_g$ is wider than $\mathrm{PSF}_z$, but if the opposite is true, we simply switch $g$ and $z$ in Equation (1) and the following. Based on the convolution theorem, the kernel function is then

$$K = \mathrm{IFT}\left\{ \frac{\mathrm{FT}\left\{\mathrm{PSF}_g\right\}}{\mathrm{FT}\left\{\mathrm{PSF}_z\right\}} \right\}, \tag{2}$$

where FT stands for the Fourier transform, and IFT is the inverse Fourier transform. However, in practice, numerical noise dominates in the high-frequency components since the ratio of $\mathrm{FT}\{\mathrm{PSF}_g\}/\mathrm{FT}\{\mathrm{PSF}_z\}$ is poorly behaved when $\mathrm{FT}\{\mathrm{PSF}_z\}$ is small. Therefore, we build a hybrid model for $\mathrm{FT}\{K\}$ where the low-frequency values are determined by $\mathrm{FT}\{\mathrm{PSF}_g\}/\mathrm{FT}\{\mathrm{PSF}_z\}$, and the high-frequency values are set to an elliptical Gaussian fit (Phillips & Davis 1995) to the frequency components. After obtaining the kernel function via the IFT, we can use Equation (1) to match the PSFs in $g$-band and $z$-band; specifically, we convolve the band with the smaller FWHM with the kernel to match the larger one of the other band.

(b) Locate the brightest pixel in the $z$-band cutout, as illustrated in Figures 1(b) and 2(b), where we labelled them by $(i_{\max}, j_{\max})$. Typically, the lens galaxy is brighter than the quasar images in $z$-band (Case 1 and Case 3). Therefore, the brightest pixel in $z$-band is where the lens galaxy is located. If Case 2 or Case 4 happens, the situation becomes the opposite, i.e., the brightest pixel in $z$-band is located at one of the quasar images.

(c) Scale the brightest pixel value in $z$-band, $z(i_{\max}, j_{\max})$, such that it becomes the same as the value in $g$-band, $g(i_{\max}, j_{\max})$, i.e., $g(i_{\max}, j_{\max}) = \alpha z(i_{\max}, j_{\max})$, where $\alpha$ is the scaling factor. After subtracting pixel values in $g$-

**Table 1**
Lens and Quasar Colors and Brightnesses

| | Case 1 (Typical) | Case 2 | Case 3 | Case 4 |
|---|---|---|---|---|
| Relative color and brightness | Quasar is bluer lens is brighter in $z$ | Quasar is bluer quasar is brighter in $z$ | Quasar is redder lens is brighter in $z$ | Quasar is redder quasar is brighter in $z$ |
| $D_1 = g - \alpha z$ (Equation (3)) | $D_1 =$ quasar images | $-D_1 =$ lens galaxy | $-D_1 =$ quasar images | $D_1 =$ lens galaxy |
| $D_2 = z - \beta D_1$ (Equation (4)) | $D_2 =$ lens galaxy | $D_2 =$ quasar images | $D_2 =$ lens galaxy | $D_2 =$ quasar images |

**Note.** Columns 2–5 are the four possible scenarios for the colors and brightnesses of the quasars and lens galaxies. We use the image cutouts in $g$-band and $z$-band labelled as $g$ and $z$ respectively. In column 1, $\alpha$ is a scaling factor which scales the brightest pixel value in $z$ to be the same as the corresponding pixel in $g$. Similarly, $\beta$ is another scaling factor which scales the brightest pixel value in $|D_1|$ to be the same as the corresponding pixel in $z$. For different cases, $D_1$ and $D_2$ yield either the lens light or the multiple images. See Section 2.1 for details.
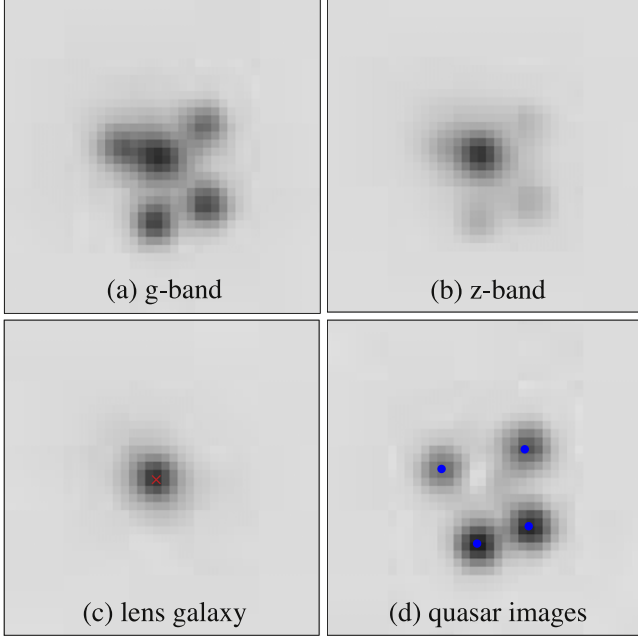


**Figure 1.** Example of a simulated quad system. Panels (a) and (b): $g$-band and $z$-band cutouts, respectively. Panels (c) and (d): the lens galaxy and the quasar images, respectively, which are separated based on color information and the procedure described in Section 2.1. The red cross in (c) is the estimated centroid of the lens light. We identify the locations of quasar images, which we indicate with the four blue dots in (d).



**Figure 2.** Example of a simulated double system. Panels (a) and (b): $g$-band and $z$-band cutouts, respectively. Panels (c) and (d): the lens galaxy and the quasar images, respectively, which are separated based on color information and the procedure described in Section 2.1. The red cross in (c) is the estimated centroid of lens light. When fitting four point sources to the quasar images in (d), the two quasar images are correctly identified by the two blue dots, whereas the remaining two blue dots are located at positions associated with noise peaks or residuals due to imperfect lens–quasar separation.

band from the scaled values in $z$-band, we obtain

$$D_1(i, j) = g(i, j) - \alpha z(i, j), \qquad (3)$$

where $i = 1 .. N_x$ and $j = 1 .. N_y$ are the pixel indices in the image cutout of dimensions $N_x \times N_y$. The image $D_1$ shows different outcomes for the four cases (Table 1). For Case 1, only quasar images are revealed in $D_1$, e.g., Figures 1(d) and 2(d). When Case 2 happens, $-D_1$ represents the lens galaxy light distribution. However, if quasar images are redder (Cases 3 and 4, which occur less frequently), quasar images are revealed in $-D_1$ for Case 3 and the lens galaxy light is defined by $D_1$ for Case 4. We summarize the outcome of image $D_1$ in Table 1.

(d) After obtaining either the quasar images or lens galaxies successfully (i.e., image $D_1$) from the previous step, we can extract the other component (i.e., the corresponding lens galaxies or quasar images, respectively) with similar procedures as in (b) and (c). We identify the brightest pixel in $|D_1(i, j)|$ as $(i'_{max}, j'_{max})$ and scale the pixel value
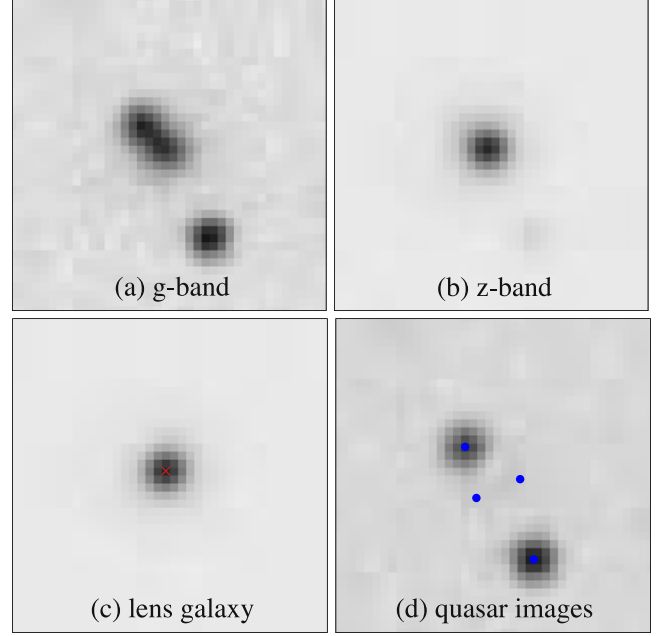
of $D_1(i'_{max}, j'_{max})$ so that it is the same as that in the $z$-band $z(i'_{max}, j'_{max})$, i.e., $z(i'_{max}, j'_{max}) = \beta D_1(i'_{max}, j'_{max})$, where $\beta$ is the scaling factor. After calculating

$$D_2(i, j) = z(i, j) - \beta D_1(i, j), \qquad (4)$$

we show as examples the resulting image $D_2$ in Figures 1 (c) and 2(c). In Table 1 we summarize the outcome of $D_2$ for each case.

In this paper, we work with objects of Case 1 or 2, i.e., the quasar images are bluer than the lens galaxy, which is the typical scenario of lens systems. To detect the rarer lens systems of Case 3 or 4, one way is to first treat all objects as Case 1 or 2, classify them (as described below in Sections 2.2–2.4), then treat all the failed Case-1 or Case-2 detections as possible Case-3 or Case-4 candidates, and classify again. This

would allow us to obtain candidates of all cases listed in Table 1.

## 2.2. Identifications of Quasar Image Positions and Lens Center

After separating the quasar images and lens galaxy, we are able to obtain $Q(i, j)$ and $L(i, j)$ from $D_1$ and $D_2$, where $Q(i, j)$ is the image containing only the quasar's light and $L(i, j)$ contains only the lens galaxy's light (see Table 1). For probing an image configuration via modeling, we have to identify image positions from $Q(i, j)$ and the lens center from $L(i, j)$.

To identify the quasar image positions, we first adopt four point sources smeared by the matched PSF to obtain the predicted image, $Q^P(i, j)$. By varying the point source positions and brightnesses, we search for the minimum difference between $Q^P(i, j)$ and $Q(i, j)$, which is defined by

$$\Delta Q^2 = \sum_{i,j} \left[ Q(i, j) - Q^P(i, j) \right]^2. \qquad (5)$$

Here we assume that the pixel uncertainty in $Q(i, j)$ is constant and thus irrelevant in the minimization for the point source positions. As shown in Figures 1(d) and 2(d), we can identify the image positions that are marked by the four blue dots. When there are only two images, two of the four dots would be located at positions associated with remaining image residuals, or at random positions when there are no significant residuals.

To estimate the lens light centroid from the distribution $L(i, j)$, we calculate the first moments of $L(i, j)$. The centroid (located at fractional rather than integral pixels) is indicated by the red cross in Figures 1(c) and 2(c).

### 2.3. Potential Quads and Doubles via Configuration

We illustrate three generic image configurations of quads and one of doubles in Figure 3: (a) cusp, (b) fold, (c) symmetric, and (d) double. In Section 2.2, we mentioned that there are two dots located at random/residual positions when fitting four dots to a double system. When the quasar images can be well separated and there is no unrelated object near the lens system, these two dots should be very faint. Therefore, we can make use of this feature to classify potential quads and doubles. Of the four identified dots, we denote $B_1$ as the brightest intensity value, $B_2$ as the second brightest, $B_3$ as the third brightest, and $B_4$ as the faintest. We further define $\theta_{12}$ as the angle subtended between the locations of $B_1$ and $B_2$ with respect to the center of the lens galaxy (see Figure 3). Based on the generic image configurations of lenses, we classify objects with $B_4/B_1 < 0.2$ and $\theta_{12} > 120°$ as potential doubles, and the remaining objects as potential quads.

### 2.4. Classification via Lens Model Fitting

After classifying the potential quads and doubles, we can model the image configurations to detect plausible lens systems. Specifically, we try to see whether the quasar images could come from a single source by varying a lens mass distribution centered close to the lens light centroid. Figure 4(a) shows an example where we can construct a lens mass model such that the quasar images could originate from the same source. In contrast, Figure 4(b) shows a configuration of quasar images where we cannot find a lens model to make the quasar images come from a single source. Following Marshall et al. (2009), we take the view that an object that can be well described by a
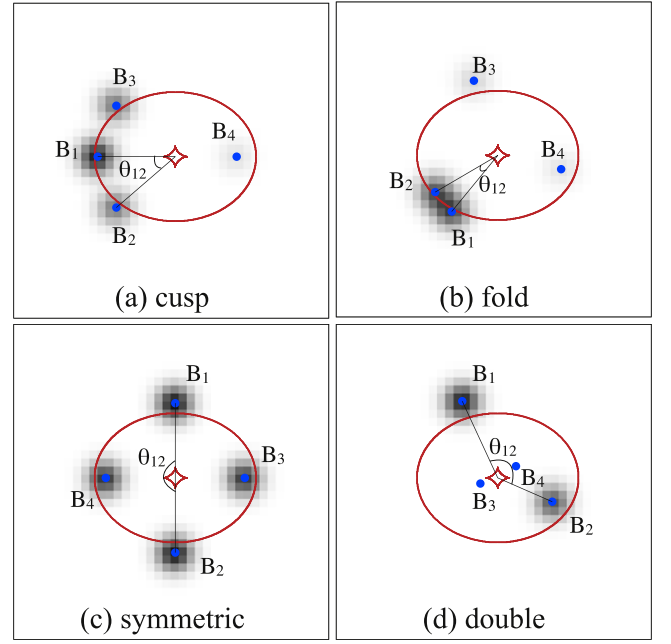


**Figure 3.** Four generic configurations of strong lens systems: (a) cusp, (b) fold, (c) symmetric, and (d) double. In each panel, the brightnesses of four images are denoted by $B_1$ to $B_4$, in the order of decreasing brightness. The angle formed by $B_1$ and $B_2$ with respect to the lens center is labeled by $\theta_{12}$. The red elliptical lines are critical lines where images are highly magnified. The red diamond-shaped lines are caustics where the critical lines map to on the source plane. Note that in (d) there are two additional images located at noise-peak/residual positions.
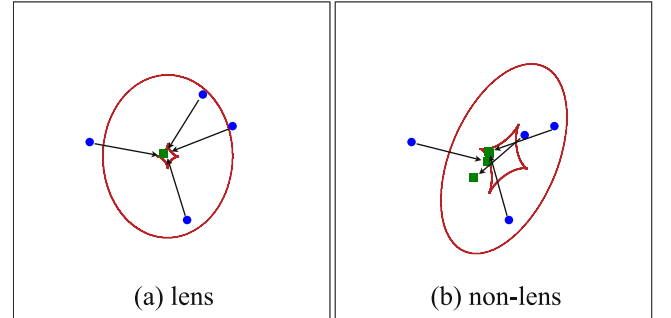


**Figure 4.** Two examples to illustrate how CHITAH classifies lens (left) and non-lens (right) systems. In both panels, the red lines are the critical lines and caustics of the best-fitting lens model. The four blue dots indicate the quasar images, and the green squares are the mapped sources of the images from the best-fitting lens model. We use the closeness of the mapped source positions to classify lens and non-lens systems: a system with quasar images that come from approximately the same source position is likely to be a lens (as in panel (a)), whereas a system with quasar images that come from distinct source positions is likely to be a non-lens (as in panel (b)).

lens model is likely to be a lens. Therefore, the lens model fitting illustrated in Figure 4 allows us to classify the left-hand object (a) as a potential lens, and discriminate the right-hand object (b) as a non-lens. In the following, we describe in detail the lens model fitting procedure.

We model the lens mass distribution as an SIE profile, whose two-dimensional surface mass density is in the form

$$\kappa(x, y) = \frac{r_{\rm ein}}{2\sqrt{x^2 + y^2/q^2}}, \qquad (6)$$

where $r_{\rm ein}$ is the Einstein radius, $q$ is the axis ratio, and $(x, y)$ are the coordinates relative to the lens center. Previous studies have shown that lens galaxies are close to having isothermal profiles (e.g., Koopmans et al. 2009; Auger et al. 2010; Barnabè et al. 2011; Oguri et al. 2014). The SIE is thus a simple profile that is adequate in describing typical image configurations of lens systems.

We define the $\chi^2_{\rm src}$ on the source (quasar) plane of the lens system as

$$\chi^2_{\rm src} = \sum_k \frac{|\boldsymbol{r}_k - \boldsymbol{r}_{\rm model}|^2}{\sigma^2_{\rm image}/\mu_k}, \qquad (7)$$

where $\boldsymbol{r}_k$ is the respective source position mapped from the position of quasar image $k$ identified in $Q(i, j)$, $\mu_k$ is the magnification at the position of quasar image $k$, and $\boldsymbol{r}_{\rm model}$ is the modeled source position evaluated as a weighted mean of $\boldsymbol{r}_k$,

$$\boldsymbol{r}_{\rm model} = \frac{\sum_k \sqrt{\mu_k} \boldsymbol{r}_k}{\sum_k \sqrt{\mu_k}} \qquad (8)$$

(Oguri 2010). Here the index $k$ runs from 1 to 4 for the quad systems, and 1 to 2 for the double systems. Since the quasar image positions are estimated through minimizing Equation (5), when adopting an imperfect PSF with a FWHM that varies by as much as $0\rlap{.}''4$ (e.g., to account for possible PSF profile mismatch), the identified image positions could deviate by at most $0\rlap{.}''2$. Therefore, we adopt conservatively the uncertainty in the identified quasar image positions, $\sigma_{\rm image}$, as $0\rlap{.}''2$.

Since we can estimate the lens center from the light profile, it is useful to use it as a constraint on the center of the SIE lens mass model because we expect the offset between the light center and the mass center of isolated lenses to be small, $\lesssim 0\rlap{.}''05$ based on previous lensing studies (e.g., Koopmans et al. 2006). Therefore, we define the $\chi^2_{\rm c}$ as

$$\chi^2_{\rm c} = \frac{|\boldsymbol{x}_{\rm model} - \boldsymbol{x}_{\rm c}|^2}{\sigma^2_{\rm c}}, \qquad (9)$$

where $\boldsymbol{x}_{\rm c}$ is the lens center from the light profile, and $\boldsymbol{x}_{\rm model}$ is the the lens center of the SIE model. Here we take $\sigma_{\rm c}$ to be also $0\rlap{.}''2$ as an estimate of the uncertainty in identifying the lens center from ground-based imaging.

We define the total goodness of fit via

$$\chi^2 = \chi^2_{\rm src} + \chi^2_{\rm c}. \qquad (10)$$

If we are able to find a lens model that can fit to the supposed lensing features of an object (with a correspondingly small value of $\chi^2$), then the object is likely to be a lens. Thus, we can set a threshold value, $\chi^2_{\rm th}$, to decide between the lens and non-lens classification: for $\chi^2 < \chi^2_{\rm th}$, we classify the object as a lens, and for $\chi^2 > \chi^2_{\rm th}$, we classify it as a non-lens. In Section 4, we explore the optimal value for the threshold.

There are four parameters for the SIE model: $r_{\rm ein}$, $q$, position angle, and lens coordinate $\boldsymbol{x}_{\rm model}$. When fitting to potential quad systems, there are four images to constrain the model. However, when fitting to potential double systems, the two images do not provide enough constraints on the SIE model, so we choose the SIS model with three parameters (i.e., the

spherical model which eliminates $q$ and the position angle parameters).

## 3. SIMULATION

To test the performance of CHITAH, we use the SIMCT[13] code from Space Warps to generate a large sample of mock quasar lenses. Space Warps is a citizen science project that looks for lenses in imaging surveys via visual inspection (Marshall et al. 2015; More et al. 2015). Details of the SIMCT framework can be found in More et al. (2015). Here, we briefly summarize the framework of SIMCT. The galaxy catalog from Gavazzi et al. (2014) is used to select massive and mostly early-type galaxies which are then parameterized as SIE lenses. Using the SIE density profile with external shear (that accounts for external mass structures along the line of sight), point images of quadruply or doubly imaged lensed quasars are generated in the CFHTLS bands ($ugriz$) with realistic colors drawn from a quasar catalog. These point sources are subsequently blurred to match the image quality of the CFHTLS images (with PSFs of FWHM of $0\rlap{.}''8$ and $0\rlap{.}''7$ for the $g$-band and $z$-band, respectively). For the profile of the PSF, we consider two forms: (1) symmetric two-dimensional Gaussian with the aforementioned FWHM, and (2) Moffat described by

$$\text{Moffat}(x, y) = \frac{\beta - 1}{\pi \alpha^2} \left[ 1 + \left( \frac{x^2 + y^2}{\alpha} \right)^2 \right]^{-\beta}, \qquad (11)$$

where $\alpha$ and $\beta$ are seeing-dependent parameters, and $(x, y)$ are the coordinates relative to the PSF center. We adopt $\alpha = 0\rlap{.}''78$ and $0\rlap{.}''69$ for $g$-band and $z$-band, respectively, and $\beta = 3.2$, which is the typical value obtained by fitting to the stars in CFHTLS (these $\alpha$ and $\beta$ values correspond to the aforementioned FWHM values). After adding noise, these simulated quasar images are then superposed on top of the images of the real galaxies that were selected to be the lenses. In total, we use $\sim 2000$ mock quads and $\sim 3000$ mock doubles for each of the two forms of the PSF as the training set. We note that our training set is different from the one described in More et al. (2015) in terms of the range of Einstein radii and the source magnitude limits. We explore a much wider range in these parameters here to test the performance of CHITAH.

Not only are simulated lenses needed, but false positives are also important for coaching CHITAH. In this work, we employ 383 "duds" from Space Warps, which are non-lensed objects that are misidentified as possible lenses by citizen scientists. These could be, for example, galaxies with several point-like star formation regions around the bulge that could be misidentified as quasar images, or the chance alignment of point sources near a galaxy.

We show some examples of the mock lenses with the Gaussian PSF and the duds in Figure 5. We categorize the mock lenses into six groups based on the quasar image separation and brightness. When the input $r_{\rm ein}$ of the mock lens is larger or smaller than $1\rlap{.}''1$, we classify the lens system as a large- or small-separation lens, respectively. Furthermore, we use the magnitude in the $z$-band of the dimmest image, $m_{\rm z}$, to separate the mock lenses into three categories: "bright," "faint,"

---

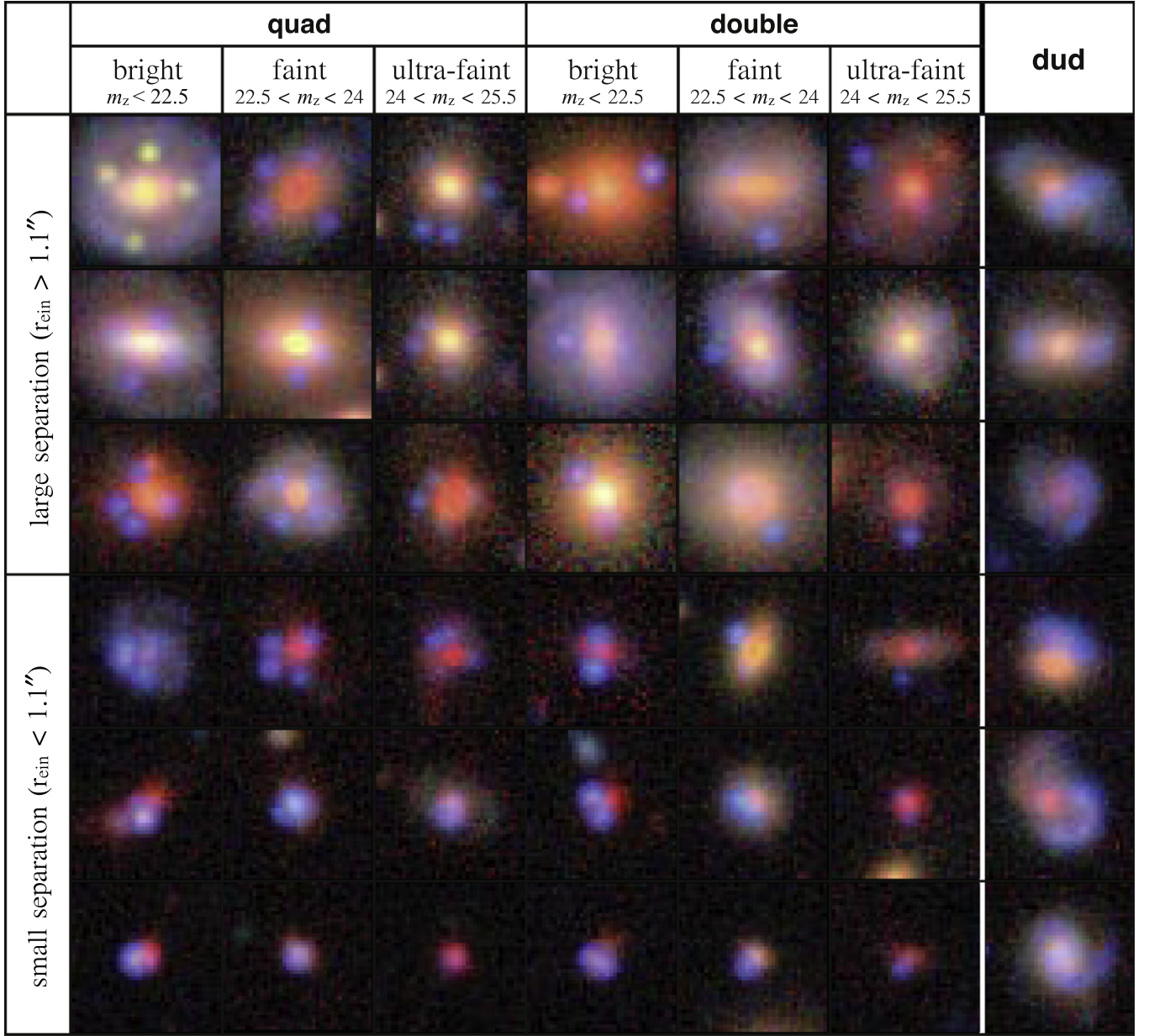[13] https://github.com/anupreeta27/SIMCT

**Figure 5.** Examples of the mock lenses (quads and doubles) with Gaussian PSF and duds used to **test** CHITAH. Using the value of $r_{ein}$ from the input SIE, we split the mock lenses into the "large separation" (with $r_{ein} > 1.\!''1$) and the "small separation" (with $r_{ein} < 1.\!''1$) samples. Based on the $z$-band AB magnitude, $m_z$, of the dimmest lensed quasar image, each of these samples is further divided into "bright" ($m_z < 22.5$), "faint" ($22.5 < m_z < 24$), and "ultra-faint" ($24 < m_z < 25.5$). In the last column we display examples of duds that are misidentified as possible lenses by citizen scientists in the Space Warps project. Each image cutout is $8'' \times 8''$.

and "ultra-faint," corresponding to $m_z < 22.5$, $22.5 < m_z < 24$, and $24 < m_z < 25.5$, respectively.

## 4. THE PERFORMANCE OF CHITAH

We investigate the performance of CHITAH in classifying the duds and simulated lenses described in the previous section. We first consider the simulations produced with the Gaussian PSF in Section 4.1, and explore the effect of the PSF in Section 4.2 by analyzing the simulations with Moffat PSFs.

### 4.1. Simulations with Gaussian PSF

To quantify the performance of CHITAH, we plot the receiver operating characteristic (ROC) curve: the relation between true- and false-positive rates. The definitions of true-positive

rate (TPR) and false-positive rate (FPR) are

$$
\text{TPR} = \frac{\text{\# of correct identifications of positive instances}}{\text{\# of positive instances}},
$$

(12)

and

$$
\text{FPR} = \frac{\text{\# of incorrect identifications of negative instances}}{\text{\# of negative instances}}.
$$

(13)

We can quantify individual TPR and FPR for the quads and doubles given the mock quads, mock doubles, and duds that we have from Section 3. For the quads, the number of positive instances is the number of mock quads, whereas the number of
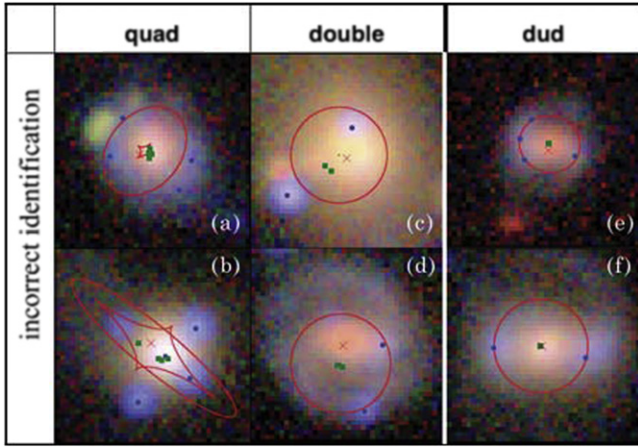
**Figure 6.** Examples of the incorrect identifications. Mock quads, mock doubles, and duds are shown in the left, middle, and right columns respectively. The mocks are generated with Gaussian PSFs. Each image cutout is $8'' \times 8''$. The red cross is the estimated centroid of the lens light. We identify the locations of quasar images, which we indicate with the four blue dots. The red elliptical lines are critical lines where lensed images are highly magnified. The red diamond-shaped lines are caustics where the critical lines map to on the source plane. The green squares are the mapped sources of the identified quasar images from the best-fitting lens model. Panel (a) shows that CHITAH misidentifies the four image positions as the blue lens light residuals rather than the faint quasar images that are in green. Panel (b) shows that CHITAH misidentifies one quasar image because of imperfect lens–quasar separation. Panel (c) shows that a large $\chi^2$ results from the two quasar images not being collinear with the lens light center, leading to an incorrect classification of this system as a non-lens. Panel (d) shows that CHITAH misidentifies the position of the fainter quasar image. Panels (e) and (f) show that the surrounding blue blobs are misidentified as quasar images that can be well fitted by an SIE/SIS model by chance.

negative instances is the number of non-quads, which is the sum of the numbers of duds and mock doubles. Similarly, for the doubles, the number of positive instances is the number of mock doubles, and the number of negative instances is the sum of the number of duds and mock quads.

We have previously illustrated correct identifications in Figure 4. Here, we show examples of incorrect identifications in Figure 6 for $\chi^2_{\rm th}$ (see Section 2.4) of 4 for quads and 1 for doubles. In each panel, the lens light centroid and the multiple quasar images that are identified by CHITAH are indicated with a red cross and blue dots, respectively. The green squares are the mapped source positions of the quasar images from the best-fitting lens model whose critical lines and caustics are shown as red elliptical lines and diamond-shaped lines, respectively. We describe the reason for the incorrect identification in each panel of Figure 6 as follows: (a) the four quasar images are misidentified at the blue lens light residuals rather than at the locations of the green blobs that are the simulated quasar images; (b) one quasar image is misidentified at the lens residual near the lens center due to imperfect lens–quasar separation; (c) the large $\chi^2$ (hence the incorrect non-lens classification) results from the two quasar images not being collinear with the lens light center; (d) one faint quasar image (near the top of the lens galaxy) is misidentified at a blue star-forming region within the spiral arms of the lens galaxy; (e) the surrounding blue ring of a galaxy is misidentified as quasar images that can be well fitted by an SIE model by chance (i.e., incorrectly identified as a quad lens); (f) the two blue star-forming regions are misidentified as quasar images that are well

fitted by an SIS model by chance (i.e., incorrectly identified as a double).

For a given value of the threshold $\chi^2_{\rm th}$ to classify between lens and non-lens (see Section 2.4), we can compute the TPR and FPR of the mock lenses and duds. A larger $\chi^2_{\rm th}$ threshold leads to both higher TPR and FPR. The reason is that it is easier to find a lens model to map the quasar positions with a $\chi^2$ value (in Equation (10)) less than the threshold $\chi^2_{\rm th}$ when $\chi^2_{\rm th}$ is large, and hence the higher TPR. At the same time, a large $\chi^2_{\rm th}$ also means that we can fit a non-lens more easily with a lens model, resulting in a higher FPR.

As shown in Figure 7, we plot the ROC curves for each of the "bright" (left-hand panel), "faint" (middle panel), and "ultra-faint" (right-hand panel) samples. Each curve is mapped out by varying $\chi^2_{\rm th}$: we start at the lower-left corner of the plot with a small $\chi^2_{\rm th}$ value, and as we increase $\chi^2_{\rm th}$, we go along the curve toward the top-right corner. The goal is to be near the top-left corner with a high TPR and a low FPR. In each curve, we mark the locations of $\chi^2_{\rm th} = 1$, 4, and 7 by circles, diamonds, and squares, respectively. For the bright quads with large separations (thick solid curve in the left-hand panel), CHITAH is able to capture these quads with a TPR $\sim 90\%$ and FPR $\sim 3\%$ when $\chi^2_{\rm th} \sim 4$. Even for the faint quads with large separations (thick solid curve in the middle panel), we obtain TPR $> 80\%$ and FPR $< 5\%$ when $\chi^2_{\rm th} \sim 4$. In general, large-separation quads (thick solid curves) are easier to identify than small-separation quads (thick dashed curves) given the higher ROC curves of large-separation quads. Also, the ROC curves of quads are closer to the top-left corner than those of doubles. This implies that CHITAH can hunt down a much purer sample of quad candidates than double candidates. According to the ROC curves, we can adopt the appropriate threshold for quad and double classifications, i.e., $\chi^2_{\rm th} \sim 4$ for quads and $\chi^2_{\rm th} \sim 1$ for doubles. We expect such threshold values to be applicable to imaging surveys that have image qualities similar to that of our mock lenses based on CFHTLS. For surveys whose image quality is different from CFHTLS, one can first simulate realistic mocks for these surveys, and then make the ROC curve to choose an appropriate $\chi^2_{\rm th}$. We note that the $\chi^2_{\rm th}$ estimated from such simulations serves as a good guide and can be tuned when applying to real data—for example, one could first choose a low $\chi^2_{\rm th}$ to get the most probable candidates when searching through an imaging survey, and then gradually relax/increase $\chi^2_{\rm th}$ to get more candidates that are likely less pure. Moreover, one can also test CHITAH on a smaller region of the actual survey, which covers previously well studied fields and where there are known lensed quasars. This will give us an idea of which $\chi^2_{\rm th}$ value provides an optimal balance between completeness and purity, and we can then apply such $\chi^2_{\rm th}$ for the entire survey.

In Figure 8, we investigate the detection sensitivity on $r_{\rm ein}$ (which is roughly half of the quasar image separation). The top panels show the TPR that is estimated with $\chi^2_{\rm th} = 4$ for quads and $\chi^2_{\rm th} = 1$ for doubles. The number of mock lenses for each $r_{\rm ein}$ bin is shown in the bottom panels. As seen from the top panels, CHITAH is able to capture quad lenses with large $r_{\rm ein}$ with nearly constant TPR as set by $\chi^2_{\rm th}$. However, we see a sharp drop in TPR as $r_{\rm ein}$ becomes smaller than $0''.5$. Small-separation lenses ($\lesssim 1''$ with $r_{\rm ein} < 0''.5$) are harder to detect since the quasar images are blended together given the PSF FWHM of
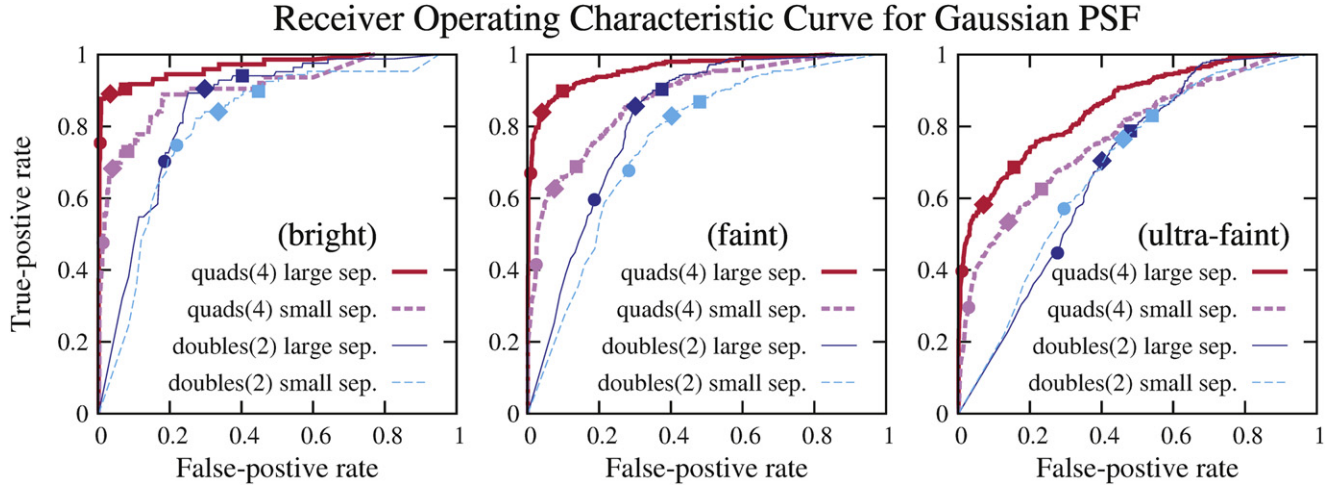
**Figure 7.** ROC curves for the mock lenses with Gaussian PSF. The three brightness groups are formed based on $m_z$ of the dimmest quasar image: bright (left-hand panel) with $m_z < 22.5$, faint (middle panel) with $22.5 < m_z < 24$, and ultra-faint (right-hand panel) with $24 < m_z < 25.5$. The thick solid and thick dashed curves display the results of mock quad lenses with large ($r_{ein} > 1\farcs1$) and small ($r_{ein} < 1\farcs1$) quasar image separations, respectively. Similarly, the thin solid and thin dashed curves show the results of mock double lenses with large and small separations, respectively. Each curve is obtained by plotting TPR vs. FPR for various $\chi^2_{th}$ settings. The locations of $\chi^2_{th} = 1$, 4, and 7 are indicated by circles, diamonds, and squares, respectively, on each curve. CHITAH is able to capture bright quads with large separations with TPR $\sim$ 90% and FPR $\sim$ 3% when $\chi^2_{th} \sim 4$, and bright doubles with large separations with TPR $>$ 70% and FPR $<$ 20% when $\chi^2_{th} \sim 1$. Large-separation quads are easier to detect than small-separation quads.
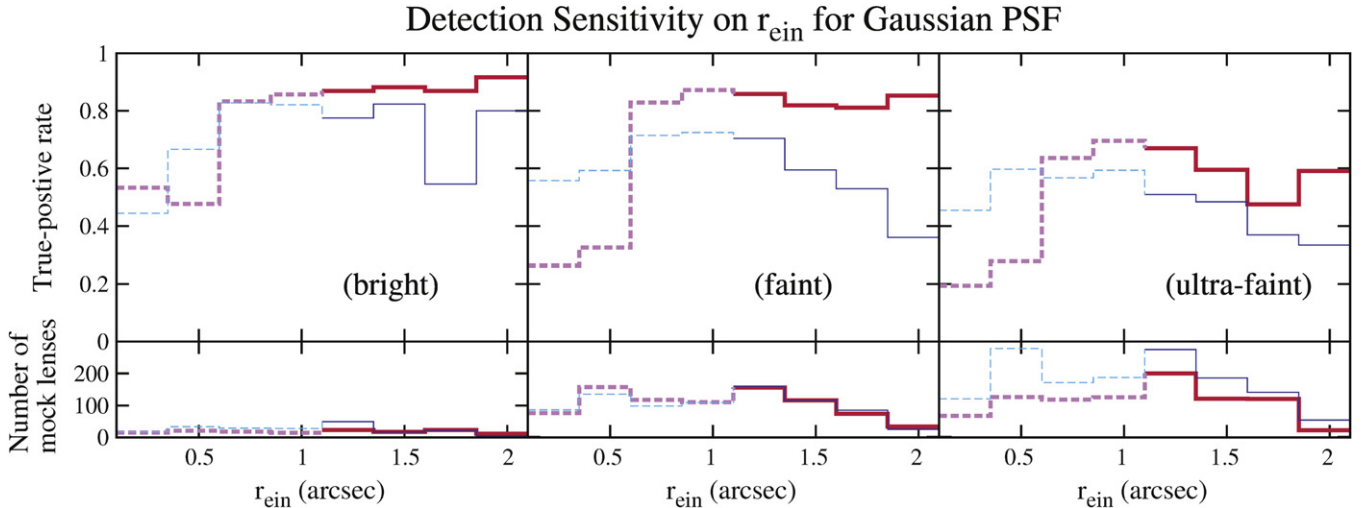


**Figure 8.** Dependence of mock-lens detection with Gaussian PSF on the input $r_{ein}$. The three brightness groups are formed based on $m_z$ of the dimmest quasar image: bright (left-hand panel) with $m_z < 22.5$, faint (middle panel) with $22.5 < m_z < 24$, and ultra-faint (right-hand panel) with $24 < m_z < 25.5$. The top panels show the detection sensitivity on $r_{ein}$, and the bottom panels are the corresponding numbers of mock lenses for each $r_{ein}$ bin. The TPR for each bin is estimated at $\chi^2_{th} = 4$ for quads and $\chi^2_{th} = 1$ for doubles. CHITAH can identify quads (thick lines) robustly for $r_{ein} \gtrsim 0\farcs5$, corresponding to the limit set by the image quality of the simulated mocks with the PSF FWHM of $0\farcs8$. There is a gradual decline in the TPR for the doubles (thin lines) as $r_{ein}$ increases due to a tendency for the lens mass center to be not collinear with the two quasar images for large $r_{ein}$ (arising from either lens ellipticity or external shear), resulting in the SIS model failing to identify such objects as lenses.

$0\farcs8$. Therefore, the performance of CHITAH in detecting small-separation quads is set by the image quality. For the doubles (thin lines), the TPR shows a decline at both small $r_{ein}$ and large $r_{ein}$. At small $r_{ein}$, it is more difficult to resolve the two quasar images, so it is harder to fit an SIS model. However, the drop in TPR for doubles is not as drastic as in that of the quads because, with only two images, it is relatively easy to use an SIS to constrain the image configurations. Note that the mock doubles with high TPR also have correspondingly high FPR ($>$20%), as is visible in Figure 7. At $r_{ein} \gtrsim 1''$, there is also a gradual decline in the TPR for the doubles as $r_{ein}$ increases. This is due to the typically larger offset between the SIS

centroid and the light centroid of the lens galaxy as the quasar image separation increases. The input mass distribution for generating the quasar image configuration is an SIE with external shear, which could lead to the two quasar images not being collinear with the lens mass center. The offset is typically larger for doubles with larger quasar image separations (i.e., larger $r_{ein}$). In contrast, the SIS model by construction has its mass center collinear with the two predicted quasar image positions. Therefore, the SIS model will tend to produce higher $\chi^2_c$ in Equation (10) for larger $r_{ein}$, causing a decline in the TPR. For the quads, the decline in TPR at large $r_{ein}$ is less apparent because we use an SIE model to fit to the quad

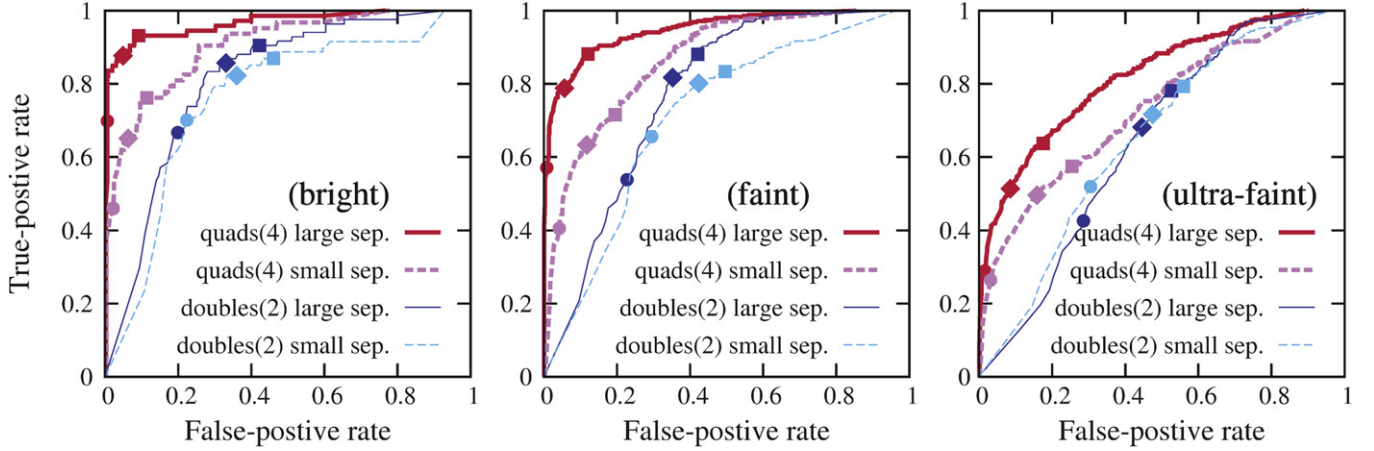## Receiver Operating Characteristic Curve for Moffat PSF



**Figure 9.** ROC curves for the mock lenses with Moffat PSF. The panels are similar to those for the Gaussian PSF mocks (Figure 7). CHITAH is able to capture bright quads with large separations with TPR $\sim 88\%$ and FPR $\sim 5\%$ when $\chi^2_{th} \sim 4$, and bright doubles with large separations with TPR $> 66\%$ and FPR $< 20\%$ when $\chi^2_{th} \sim 1$. In comparison with the ROC curves for Gaussian mocks, the Moffat PSF leads to a lower ROC curve at the level of a few percent.

## Detection Sensitivity on $r_{ein}$ for Moffat PSF
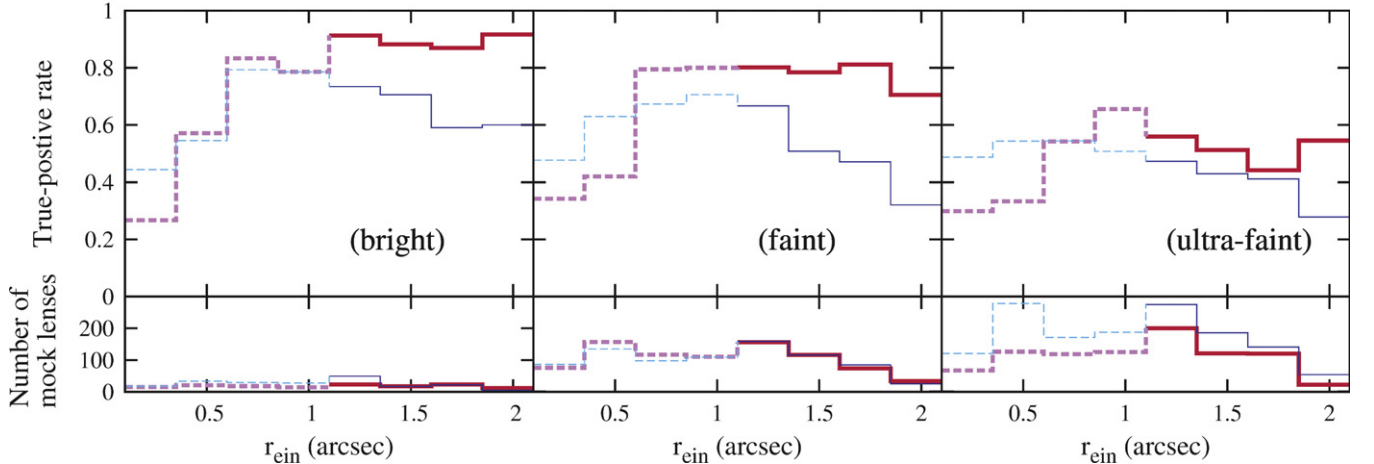


**Figure 10.** Dependence of mock-lens detection on the input $r_{ein}$ for mocks with Moffat PSF. The three brightness groups are formed based on $m_z$ of the dimmest quasar image: bright (left-hand panel) with $m_z < 22.5$, faint (middle panel) with $22.5 < m_z < 24$, and ultra-faint (right-hand panel) with $24 < m_z < 25.5$. The top panels show the detection sensitivity on $r_{ein}$, and the bottom panels are the corresponding numbers of mock lenses for each $r_{ein}$ bin. The TPR for each bin is estimated at $\chi^2_{th} = 4$ for quads and $\chi^2_{th} = 1$ for doubles. The panels are similar to those for Gaussian PSF mocks, but TPRs decrease by $\sim 5\%$ due to the more extended wings of the Moffat PSF.

configuration and the effect of the external shear can be mostly absorbed into a change in the ellipticity of the SIE to yield a low $\chi^2$.

### 4.2. Simulations with Moffat PSF

To further explore the effect of the PSF, we generalize the Gaussian PSF to the Moffat function defined in Equation (11), which describes better the wings of PSFs in CFHTLS observations. After running CHITAH on the same data set of mocks with Moffat PSF, we plot the ROC curves and the detection sensitivities of $r_{ein}$ for each sample as shown in Figures 9 and 10, respectively.

The results for Moffat PSF have very similar features to those for Gaussian PSF, although slightly worse due to the more extended wings of the Moffat PSF. For the mocks with Moffat PSF, CHITAH is able to reach TPR $\sim 88\%$ and FPR $\sim 5\%$ when $\chi^2_{th} \sim 4$ for the bright quads with large

separations (thick solid curve in the left-hand panel). As a result of the extended PSF wing effect, we notice that the ROC curves for Moffat PSF become slightly lower. The TPRs decline by $\sim 2\%$ for the bright quasar sample, and by $\sim 7\%$ for the ultra-faint quasar sample. Based on this simple test, it appears that the form of the PSF has an effect on the ROC at the level of a few percent. We also note the importance of having good PSF models in imaging suveys in order to match the PSFs of different bands. In short, CHITAH performs best for quad lens systems with bright and widely separated quasars and with narrow and well characterized PSFs.

## 5. APPLICATION TO COSMOS 5921+0638

To demonstrate that CHITAH not only captures simulated lenses but also real lenses, we consider the known gravitational lens COSMOS 5921+0638 in this section.
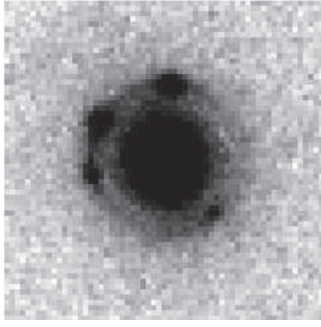
**Figure 11.** *HST* ACS F814W exposure cutout image of COSMOS 5921+0638, discovered by Faure et al. (2008). The elliptical galaxy at the center is the lens galaxy, and four lensed quasar images are located around the lens. The pixel scale is 0″.05 and the field of view is 3″ × 3″. The cutout image is obtained from the data release of Faure et al. (2008).

### 5.1. Observations of COSMOS 5921+0638

The lens system COMOS 5921+0638 is one of the 67 strong lens candidates discovered by Faure et al. (2008) via visual inspection of early-type galaxies with redshifts <1.0 in the 1.64 deg$^2$ *HST* COSMOS survey (Scoville et al. 2007). The *HST* ACS F814W exposure of COSMOS 5921+0638, obtained from the data release by Faure et al. (2008),[14] is shown in Figure 11. Anguita et al. (2009) obtained spectroscopic follow-up observations and performed a detailed analysis of the lensing system COSMOS 5921+0638. They have confirmed that COSMOS 5921+0638 is a lensed quasar and not a lensed galaxy based on the morphology, i.e., the four point-like images that lie around an early-type galaxy suggest that the background source is a quasar. They also measured the lens redshift to be $z_l = 0.551$ from FORS1 observations and inferred a possible AGN source redshift of $z_s = 3.14$ from the $u^*$ drop-out criterion and a candidate Ly-alpha line. Anguita et al. (2009) found that an SIE with a small amount of external shear ($\gamma = 0.038$) provides an adequate fit to the observed positions of the quasar images in COSMOS 5921+0638.

We attempt to feed CHITAH this lensed quasar system to test its ability. We use the ground-based images of COSMOS 5921+0638 from the Suprime-Cam on the 8.2 m Subaru Telescope (Taniguchi et al. 2007). The optical images are obtained in six broadbands: *B*, *g′*, *V*, *r′*, *i′* and *z′*. We obtained the images from the Subaru archive and reduced the images using the HSC pipeline, a derivative of the LSST pipeline[15](Ivezic et al. 2008; Axelrod et al. 2010), modified for use with Suprime-Cam and Hyper Suprime-Cam. The images were overscan-subtracted, flat-fielded using the COSMOS flats[16] and calibrated against the Eighth Data Release of the Sloan Digital Sky Survey (Aihara et al. 2011). These calibrated images were warped to a common coordinate system and combined with mild clipping (3σ, 2 iterations) to reject extreme outliers. The aperture photometry on the coadd has an rms difference of ~4% in *r*-band against SDSS, and the astrometry rms difference is 100 mas.

---

[14] http://wwwstaff.ari.uni-heidelberg.de/mitarbeiter/cfaure/cosmos/info/info.5921+0638.html
[15] https://confluence.lsstcorp.org/display/LSWUG/LSST+Software+User+Guide
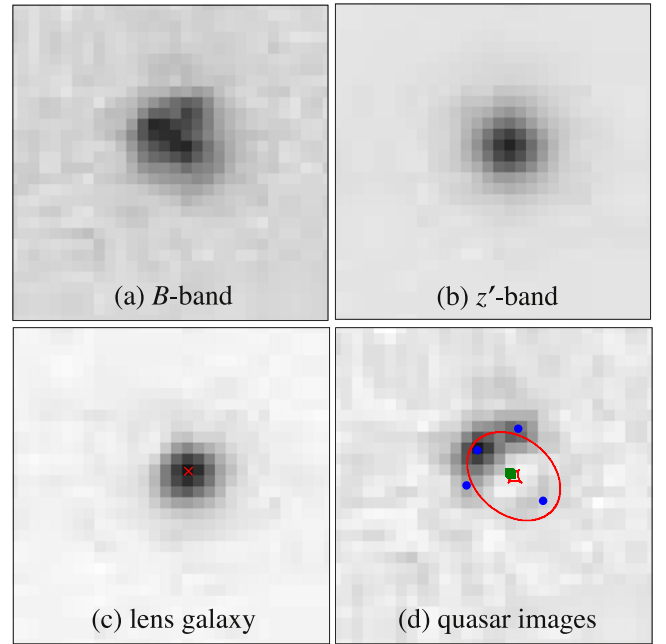[16] http://irsa.ipac.caltech.edu/data/COSMOS/images/subaru/flats



**Figure 12.** Classification of COSMOS 5921+0638 by CHITAH. Panels (a) and (b): *B*- and *z′*-band cutouts, respectively. Panels (c) and (d): the lens galaxy and the quasar images, respectively, which are separated based on color information and the procedure described in Section 2.1. The red cross in (c) is the estimated centroid of lens light. We identify the locations of quasar images, which we indicate with the four blue dots in (d). The red elliptical lines are *critical lines* where images are highly magnified. The tiny red diamond-shaped lines near the center are *caustics* where the critical lines map to on the source plane. The green squares are the mapped sources of each image from the best-fitting lens model. The closeness of all the mapped sources indicates that COSMOS 5921+0638 is indeed a lensed system.

The *B*- and *z′*-band image cutouts are illustrated in Figures 12(a) and (b), respectively. The pixel scale is 0″.20. We estimate the PSF FWHM to be ~0″.55 for *B*-band and ~0″.8 for *z′*-band by fitting symmetric two-dimensional Gaussians to stars in the field.

### 5.2. CHITAH on COSMOS 5921+0638

To separate the lens and images more effectively, we choose the cutouts in the bluest band and in the reddest band, i.e., the *B*- and *z′*-bands. The performance of CHITAH is illustrated in Figure 12. We can separate cleanly the lens galaxy light (panel (c)) and quasar images (panel (d)). We can also classify COSMOS 5921+0638 as Case 1 (where the quasar images are bluer than the lens galaxy and the lens galaxy is brighter than the quasar images in the *z′*-band). After separation of lens and quasars, we are able to identify image positions labeled by the four blue dots in Figure 12(d). The lens centroid is also estimated and labeled as a red cross in Figure 12(c). We can fit an SIE model to the observed image configuration; as shown in Figure 12(d), the mapped sources from the quasar images lie close together with a $\chi^2 \sim 0.53$, and the Einstein radius of the best-fit SIE model is $r_{ein} \sim 0″.74$, which is comparable to the Einstein radius (0″.71) measured by Anguita et al. (2009). To categorize COSMOS 5921+0638, we estimate the signal-to-noise ratio (SNR) of the faintest quasar image in *z′*-band/*z*-band for both COSMOS and CFHTLS based on the smeared $m_z$ brightness, because the COSMOS depth differs from that of the CFHTLS. The SNR of COSMOS 5921+0638 is ~8, which can be classified in the faint group, $29 \gtrsim SNR_{CFHTLS} \gtrsim 7$

(corresponding to $22.5 < m_z < 24$ for CFHTLS). Therefore, CHITAH is able to detect COSMOS 5921+0638, a faint small-separation quad, as a lens candidate successfully.

## 6. SUMMARY AND DISCUSSIONS

We have built a novel robot, CHITAH, to classify lensed candidates in imaging surveys via modeling of the image configuration. We use simulated CFHTLS-Wide-like lens systems from Space Warps to study the performance of CHITAH. The classification strategy is divided into four steps. First of all, we disentangle lens galaxy light and multiple quasar images using color information. Second, we measure the lens center and the quasar image positions. Third, through the quasar image configuration, we separate the targets into two groups: potential quads and potential doubles. Lastly, we model the potential quad/double image configuration via an SIE/SIS lens distribution, and use the resulting $\chi^2$ from the model to classify the lens. We can choose an appropriate value for the $\chi^2_{\rm th}$ to separate lens and non-lens classifications (objects with $\chi^2 < \chi^2_{\rm th}$ are classified as lenses whereas objects with $\chi^2 > \chi^2_{\rm th}$ are classified as non-lenses).

After *testing* CHITAH on simulated CFHTLS-Wide-like data we draw the following conclusions.

1. The optimal threashold of $\chi^2_{\rm th}$ can be set to $\chi^2_{\rm th} \sim 4$ for quad classification, and $\chi^2_{\rm th} \sim 1$ for double selection for imaging surveys with image qualities similar to that of CFHTLS.
2. CHITAH can hunt down much purer lens candidates for quads than doubles.
3. For bright quads with large image separations ($r_{\rm ein} > 1''1$) simulated with Gaussian PSFs, we achieve a high TPR ($\sim$90%) and a low FPR ($\sim$3%). For the faint large-separation quads, CHITAH is also able to detect them very well with TPR > 80% and FPR < 5%.
4. We detect a sharp drop of TPR as $r_{\rm ein}$ becomes smaller than $\sim$0''5 (i.e., with quasar image separations $\lesssim 1''$), which corresponds roughly to the PSF seeing of the mock lenses. The performance of CHITAH is thus set by the image quality.
5. Relative to the Gaussian PSF, the extended wings of Moffat PSF decrease the TPRs by a few percent.
6. We feed the real lens system COSMOS 5921+0638 to CHITAH, and CHITAH successfully classifies it as a quad system.

Having a fast CHITAH for lens classification is one of our goals of the robot development. Based on the simple yet robust scheme (outlined in Section 2), CHITAH takes about 5 s to classify one object on an Intel i7 3.2 GHz CPU. This translated to about a week to search through a million objects with an 8-core CPU.

To achieve a fast strategy, we simply employ the source plane $\chi^2_{\rm src}$ in Equation (7), and add the lens light center as prior $\chi^2_{\rm c}$ in Equation (9). Despite the simplicity, we can detect lens candidates with high TPR and low FPR based on our simulations. A possible way to enhance the algorithm even further would be to obtain $\chi^2_{\rm src}$ by considering the full magnification tensor (e.g., see Appendix 2 of Oguri 2010). Flux ratios are possible additional observational constraints for modeling, although the flux ratio uncertainty would need to accommodate the typical anomalous quasar flux ratios.

Moroeover, the ellipticity and position angle of the lens light profile may also be added as priors, but the complexity may slow down the efficiency of the algorithm. For exotic lenses that cannot be readily described by an SIE profile, one may also equip CHITAH with other lens models, or use additional bands (e.g., near-infrared) or different band combinations to identify better these rarer lensed objects. Exotic lenses are generally difficult to find with automated algorithms, and are usually easier to spot via visual inspections, such as through Space Warps.

Current surveys such as the HSC survey and DES are imaging a wide area of the sky (thousands of square degrees) in multiple bands, and in the future the LSST will image the entire southern sky. HSC, DES, and LSST have similar imaging bands to the CFHTLS-Wide-like lenses considered in this paper, so CHITAH is readily applicable to these current/future imaging surveys. There will be hundreds of new quasar lens systems in these ongoing surveys and thousands of quasar lenses in LSST (Oguri & Marshall 2010), increasing the existing sample by at least two orders of magnitude. We expect CHITAH to be a good and efficient hunter of new lenses in these surveys.

## REFERENCES

Agnello, A., Kelly, B. C., Treu, T., & Marshall, P. J. 2015, MNRAS, 448, 1446
Aihara, H., Allende Prieto, C., An, D., et al. 2011, ApJS, 193, 29
Anguita, T., Faure, C., Kneib, J.-P., et al. 2009, A&A, 507, 35
Auger, M. W., Treu, T., Bolton, A. S., et al. 2010, ApJ, 724, 511
Axelrod, T., Kantor, J., Lupton, R. H., & Pierfederici, F. 2010, Proc. SPIE, 7740, 774015
Barnabè, M., Czoske, O., Koopmans, L. V. E., Treu, T., & Bolton, A. S. 2011, MNRAS, 415, 2215
Bolton, A. S., Burles, S., Koopmans, L. V. E., Treu, T., & Moustakas, L. A. 2006, ApJ, 638, 703
Brownstein, J. R., Bolton, A. S., Schlegel, D. J., et al. 2012, ApJ, 744, 41
Cabanac, R. A., Alard, C., Dantel-Fort, M., et al. 2007, A&A, 461, 813
Courbin, F., Chantry, V., Revaz, Y., et al. 2011, A&A, 536, A53
Dalal, N., & Kochanek, C. S. 2002, ApJ, 572, 25
Faure, C., Kneib, J.-P., Covone, G., et al. 2008, ApJS, 176, 19
Gavazzi, R., Marshall, P. J., Treu, T., & Sonnenfeld, A. 2014, ApJ, 785, 144
Gavazzi, R., Treu, T., Marshall, P. J., Brault, F., & Ruff, A. 2012, ApJ, 761, 170

Inada, N., Oguri, M., Becker, R. H., et al. 2008, AJ, 135, 496
Inada, N., Oguri, M., Shin, M.-S., et al. 2010, AJ, 140, 403
Inada, N., Oguri, M., Shin, M.-S., et al. 2012, AJ, 143, 119
Ivezic, Z., Tyson, J. A., Abel, B., et al. 2008, arXiv:0805.2366
Jackson, N., Rampadarath, H., Ofek, E. O., Oguri, M., & Shin, M.-S. 2012, MNRAS, 419, 2014
Jee, I., Komatsu, E., & Suyu, S. H. 2014, arXiv:1410.7770
Kochanek, C. S., Morgan, N. D., Falco, E. E., et al. 2006, ApJ, 640, 47
Koopmans, L. V. E., Bolton, A., Treu, T., et al. 2009, ApJL, 703, L51
Koopmans, L. V. E., Treu, T., Bolton, A. S., Burles, S., & Moustakas, L. A. 2006, ApJ, 649, 599
Marshall, P., Verma, A., More, A., et al. 2015, arXiv:1504.06148
Marshall, P. J., Hogg, D. W., Moustakas, L. A., et al. 2009, ApJ, 694, 924
Miyazaki, S., Komiyama, Y., Nakaya, H., et al. 2012, Proc. SPIE, 8446, 84460Z
More, A., Cabanac, R., More, S., et al. 2012, ApJ, 749, 38
More, A., Verma, A., Marshall, P., et al. 2015, arXiv:1504.05587
Myers, S. T., Jackson, N. J., Browne, I. W. A., et al. 2003, MNRAS, 341, 1
Negrello, M., Hopwood, R., De Zotti, G., et al. 2010, Sci, 330, 800
Oguri, M. 2010, PASJ, 62, 1017
Oguri, M., Inada, N., Pindor, B., et al. 2006, AJ, 132, 999
Oguri, M., Inada, N., Strauss, M. A., et al. 2008, AJ, 135, 512
Oguri, M., Inada, N., Strauss, M. A., et al. 2012, AJ, 143, 120
Oguri, M., & Marshall, P. J. 2010, MNRAS, 405, 2579
Oguri, M., Rusu, C. E., & Falco, E. E. 2014, MNRAS, 439, 2494
Paraficz, D., & Hjorth, J. 2009, A&A, 507, L49
Phillips, A. C., & Davis, L. E. 1995, in ASP Conf. Ser. 77, Astronomical Data Analysis Software and Systems IV, ed. R. A. Shaw, H. E. Payne & J. J. E. Hayes (San Francisco, CA: ASP), 297
Refsdal, S. 1964, MNRAS, 128, 307
Sánchez, E., & DES Collaboration 2010, JPhCS, 259, 012080
Scoville, N., Abraham, R. G., Aussel, H., et al. 2007, ApJS, 172, 38
Suyu, S. H., Auger, M. W., Hilbert, S., et al. 2013, ApJ, 766, 70
Suyu, S. H., Hensel, S. W., McKean, J. P., et al. 2012, ApJ, 750, 10
Suyu, S. H., Marshall, P. J., Auger, M. W., et al. 2010, ApJ, 711, 201
Taniguchi, Y., Scoville, N., Murayama, T., et al. 2007, ApJS, 172, 9
Tewes, M., Courbin, F., & Meylan, G. 2013, A&A, 553, A120
Vegetti, S., Lagattuta, D. J., McKean, J. P., et al. 2012, Natur, 481, 341
Vieira, J. D., Marrone, D. P., Chapman, S. C., et al. 2013, Natur, 495, 344
Walsh, D., Carswell, R. F., & Weymann, R. J. 1979, Natur, 279, 381